Compressive Behavior of Large-Scale PEN and PET FRP–Confined RC Columns with Square Cross Sections

Yu-Lei Bai[1]; Yu-Feng Zhang[2]; Jun-Feng Jia[3]; Qiang Han[4]; Xiu-Li Du[5]; and Togay Ozbakkaloglu, M.ASCE[6]

Abstract: This paper presents results of a first-ever experimental study on the axial compressive behavior of large-scale square reinforced concrete (RC) columns confined with polyethylene naphthalate (PEN)/terephthalate (PET) fiber–reinforced polymer (FRP) composites, which is a new type of FRP with a large rupture strain (LRS) of over 5%. In total, 10 large-scale square RC columns were tested under axial compression, including 8 LRS FRP–wrapped RC columns and 2 RC columns, which served as control specimens. The key experimental parameters were the sectional corner radius and the thickness and type of LRS FRP. The test results show that the effective confinement stiffness ratio of an FRP jacket, as determined by the corner radius and FRP thickness, has a significant effect on the axial compressive behavior of LRS FRP–jacketed large-scale square RC columns. Based on the experimental results, this paper presents an evaluation of two existing LRS FRP–confined concrete models for noncircular columns. Finally, based on the test findings, a refined model for LRS FRP–confined large-scale square columns is presented to provide more accurate predictions of the compressive behavior of these columns.
DOI: 10.1061/(ASCE)CC.1943-5614.0001222.

Author keywords: Polyethylene naphthalate/terephthalate fiber–reinforced polymer; Large rupture strain; Reinforced concrete; Large-scale test; Square; Compressive behavior.

Introduction

External wrapping with fiber-reinforced polymer (FRP) composites is a commonly accepted strategy to enhance the mechanical properties of core concrete in terms of both strength and deformability (Lam and Teng 2003a, b; Wang and Wu 2008; Wang et al. 2012, 2016; Li et al. 2018; Liao et al. 2021). In the last three decades, substantial research has investigated the compression response of FRP-wrapped circular and noncircular specimens, resulting in a large number of FRP–confined concrete stress–strain models (Ozbakkaloglu 2013a, b; Ozbakkaloglu et al. 2013; Pimanmas and Saleem 2019; Lin and Teng 2020; Bai et al. 2019, 2021b). However, most of these investigations concentrated on columns confined with carbon FRP (CFRP), glass FRP (GFRP), or aramid FRP (AFRP), while studies examining the compressive behavior of large-scale specimens have remained limited (Wang and Restrepo 2001; Toutanji et al. 2010; De Luca, et al. 2011; Zeng et al. 2018, 2021). The aforementioned FRPs have a linear elastic stress–strain relationship, a high elastic modulus, and a small ultimate tensile fracture strain (less than 3%), which are commonly referred to as conventional FRPs (Bai et al. 2019; Pimanmas and Saleem 2019). Polyethylene naphthalate (PEN) and polyethylene terephthalate (PET) FRPs are two newly developed environmentally friendly material made of scrap plastic products, and the ultimate tensile fracture strain of PEN and PET FRP is larger than 5%. Because of their large fracture strain properties, the two kinds of FRPs are usually called large rupture strain (LRS) FRPs. Compared with conventional FRPs, the LRS FRP exhibits a much lower two-stage tensile stiffness but a much larger strain ability, as seen in Fig. 1. Some recent studies on the compressive behavior of LRS FRP–confined cylinders have demonstrated the superior ductility and energy absorption in LRS FRP–confined concrete (Dai et al. 2011; Ispir 2015; Huang et al. 2018; Ispir et al. 2018; Bai et al. 2014, 2019; Han et al. 2020b; Saleem et al. 2017, 2021; Yuan et al. 2021). The attributes of LRS FRP research also extend to the seismic response of LRS FRP–jacketed specimens (Anggawidjaja et al. 2006; Dai et al. 2012; Zhou et al. 2020). The LRS FRP has become a highly attractive alternative for contractors seeking ductility enhancement as the key to improved seismic strengthening.

In comparison with circular columns, square and rectangular columns are more prevalent in building applications in practice. Previous research has shown that, compared with circular columns, FRP confinement in square or rectangular columns is poorer because of the existence of their acute edges and nonuniform stress distribution. The effectiveness of FRP confinement increases with the corner radius (Lam and Teng 2003b; Wang et al. 2016; Zeng et al. 2018; Lin and Teng 2020). The compression behavior of confined concrete is closely related to its external jacketing materials. The bilinear tensile properties of the LRS FRP are obviously different from conventional FRPs. Thus, the compressive behavior of LRS FRP–confined concrete in noncircular columns needs to be

[1]Professor, Key Laboratory of Urban Security and Disaster Engineering of Ministry of Education, Beijing Univ. of Technology, Beijing 100124, China. Email: baiyulei@bjut.edu.cn

[2]Ph.D. Candidate, Key Laboratory of Urban Security and Disaster Engineering of Ministry of Education, Beijing Univ. of Technology, Beijing 100124, China. ORCID: https://orcid.org/0000-0003-3386-4975. Email: yfzbjut@163.com

[3]Professor, Key Laboratory of Urban Security and Disaster Engineering of Ministry of Education, Beijing Univ. of Technology, Beijing 100124, China (corresponding author). Email: jiajunfeng@bjut.edu.cn

[4]Professor, Key Laboratory of Urban Security and Disaster Engineering of Ministry of Education, Beijing Univ. of Technology, Beijing 100124, China. ORCID: https://orcid.org/0000-0002-1664-3065. Email: qhan@bjut.edu.cn

[5]Professor, Key Laboratory of Urban Security and Disaster Engineering of Ministry of Education, Beijing Univ. of Technology, Beijing 100124, China. Email: duxiuli@bjut.edu.cn

[6]Professor, Ingram School of Engineering, Texas State Univ., San Marcos, TX 78667. Email: togay.oz@txstate.edu

Note. This manuscript was submitted on September 8, 2021; approved on March 13, 2022; published online on May 11, 2022. Discussion period open until October 11, 2022; separate discussions must be submitted for individual papers. This paper is part of the ***Journal of Composites for Construction***, © ASCE, ISSN 1090-0268.

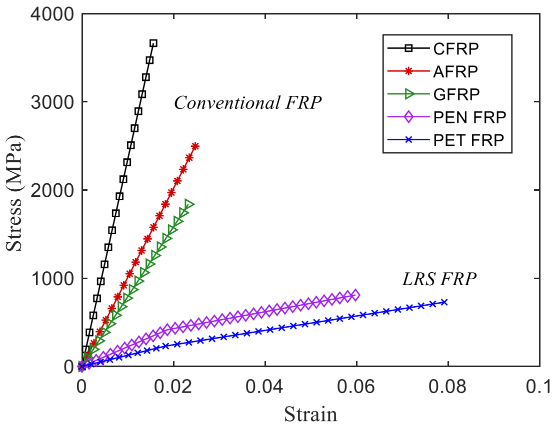

Fig. 1. Typical tensile stress–strain curves of a conventional and an LRS FRP.

examined. However, existing experimental investigations on LRS FRP–wrapped noncircular specimens are very limited and have focused only on small-scale specimens (Pimanmas and Saleem 2018, 2019; Han et al. 2020a; Saleem et al. 2017, 2021). The most recent research shows how LRS FRP–confined noncircular columns feature a high degree of ductile performance, and the sharp corners' knife action is substantially restricted due to the large elongation of the LRS FRP. Moreover, the stress–strain response of noncircular columns wrapped with LRS FRP exhibits a trilinear stress–strain relationship, which is different from the bilinear stress–strain curves of noncircular columns confined with conventional FRPs (Pimanmas and Saleem 2019; Han et al. 2020a).

For the soundness of design of noncircular RC columns with LRS FRP jackets in seismic retrofitting applications, an accurate prediction of the compressive behavior of a large-scale LRS FRP–confined column with a noncircular section is essential. To date, only two studies have proposed an axial stress–strain model for LRS FRP–confined noncircular concrete columns (Pimanmas and Saleem 2019; Zhang 2021). In addition, most previous experimental research has shown that the column size effect is marginal for FRP-wrapped circular columns with a sufficient confinement level (Matthys et al. 2005; Silva and Rodrigues 2006; Zhou and Wu 2012). Nevertheless, size effect may play an important role for FRP-wrapped noncircular columns (De Luca, et al. 2011; Zeng et al. 2018; Chan et al. 2021). Therefore, the reliability and applicability of these stress–strain models that were developed on the basis of data obtained on small-scale noncircular columns for LRS FRP–confined large-scale noncircular columns need to be carefully checked.

Against this background, the current paper presents a test program on the axial compressive response of LRS FRP–jacketed large-scale square RC columns. Following the test program, a discussion on the effects of the major test variables is initiated. Finally, the experiment results are used to evaluate two existing stress–strain models for LRS FRP–confined concrete in noncircular columns, and then a refined model with an improved prediction accuracy is presented for LRS FRP–wrapped large-scale square columns.

Experimental Program

Test Specimens

In this paper, a total of 10 RC specimens were manufactured and tested subjected to axial compression. Among them, eight columns were confined specimens, and the remaining two unwrapped columns acted as control specimens. All the columns had a section size ($b \times h$, width and length of the cross section) of 400×400 mm and a height of 1,200 mm. The main parameters considered were the corner radius, FRP types, and FRP jacket thickness. Details of the test columns are shown in Fig. 2 and listed in Table 1. These specimens were divided into two groups on the basis of the corner radius (r) (Lim and Ozbakkaloglu 2014; Zeng et al. 2018; Li et al. 2019; Lin and Teng 2020). The specimens in Groups 1 and 2 had a corner radius of 50 and 80 mm, resulting in two corner radius ratios ($r_c = 2r/h$) of 0.25 and 0.4, respectively. In addition, two types of LRS FRP, namely, PEN FRP and PET FRP, were used to jacket the target columns; hence, two, three, and four layers of PEN FRP were adopted to study the influence of the jacket stiffness (i.e., the FRP jacket's product of elastic modulus and thickness). Due to the relatively low elastic modulus of PET FRP, six layers of PET FRP were designed to compare with three layers of PEN FRP, aiming to study the influence of different rupture strains on FRP-wrapped columns when the jacket stiffnesses are similar (Table 1).

As shown in Fig. 2(a), all columns were longitudinally reinforced with eight deformed steel bars 22 mm in diameter and transversely reinforced with round steel bars 8 mm in diameter. The specimens in Groups 1 and 2 had a longitudinal steel reinforcement ratio (ρ_{sc}) of 1.93% and 1.97%, respectively. Such a slight difference was due to the different corner radii of the two sets of specimens, leading to a slight difference in the cross-sectional area. Each column had a middle height test area of 700 mm and a 250-mm loading area at both ends. The transverse reinforcements were spaced 50–100 mm–100 mm at the top and bottom loading areas of the specimen. This region was a densely transversely reinforced area designed to avoid unexpected end failure. The spacing of the transverse reinforcements was designed to be relatively large in the test region to reduce their confinement effect. However, as per ACI 318-19 (ACI 2019), their spacing range should not be greater than 16 times the diameter of the longitudinal bars (352 mm). Therefore, a spacing of 200–300–200 mm (longitudinal bar slenderness ratio of 9.1–13.6–9.1) was used in the middle test region [Fig. 2(a)]. The concrete cover thickness was 50 mm, measured from the surface of the square section to the center of the longitudinal steel bars [Fig. 2(b)].

For ease of reference, each specimen in this research was assigned a name according to the following rules: (1) the initial r represents the corner radius, followed by the numbers, 50 or 80, to denote the different corner radii; (2) PEN or PET indicates the FRP types, followed by the number of FRP layers. For example, *r50-PEN-2* refers to the specimen that has a 50- mm corner radius and a two-layer PEN FRP, and *r50* refers to the corresponding control specimen without FRP wrapping.

Preparation of Specimens

First, the longitudinal reinforcements were welded to the 20-mm-thick steel plates at both ends; then, the transverse reinforcements were installed to form a reinforcement cage [Fig. 3(a)]. Wooden molds served as the outer formwork of the specimens [Fig. 3(b)]. Before casting concrete, proper measures were taken to ensure that the steel cage and the wooden molds were assembled accurately. The seams at the bottom of the wooden molds were sealed by silicone gel to prevent water leakage. The strain gauges (SGs) mounted on the steel bars were secured with waterproof coating adhesive. All columns were cast using one batch of commercial concrete supplied by a local plant with a maximum coarse aggregate size of 25 mm. The concrete was then poured into the formwork via the opening in its top steel plate and the formwork was removed after ten days of concrete curing.

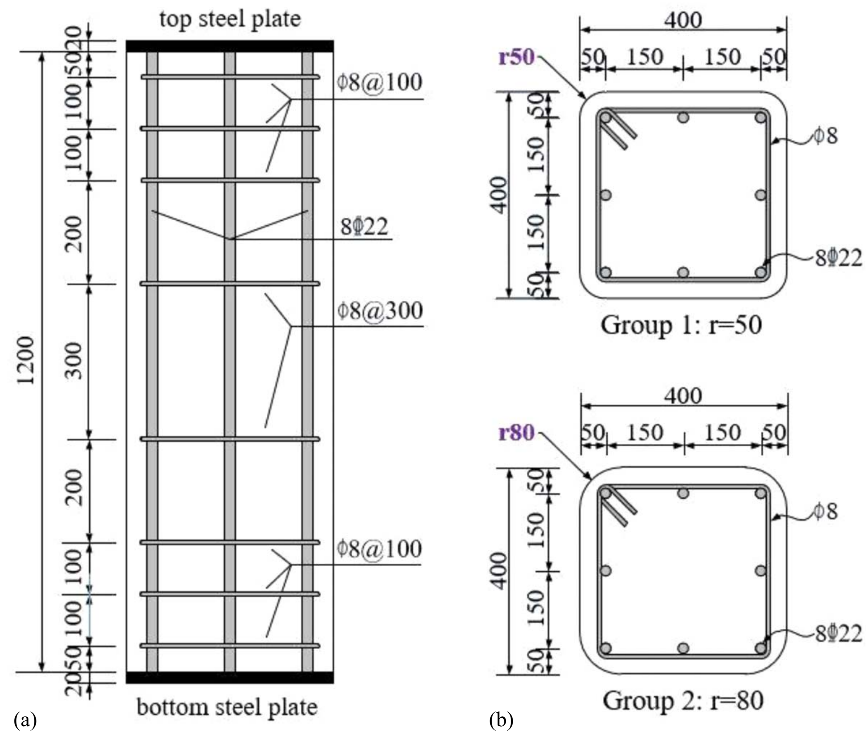

Fig. 2. Geometry and reinforcement details of test columns (unit: mm): (a) longitudinal section; and (b) cross section.

Table 1. Test specimens

No.	Specimen	Cross section ($b \times h$) (mm)	Group	Corner radius, r (mm)	Corner radius ratio, r_c	FRP type	FRP layers N_{frp}	Nominal thickness of FRP t_{frp} (mm)	FRP reinforcement ratio, ρ_f (%)
1	r50	400 × 400	1	50	0.25	Control specimen	—	—	0
2	r50-PEN-2	400 × 400		50	0.25	PEN	2	2.544	2.44
3	r50-PEN-3	400 × 400		50	0.25	PEN	3	3.816	3.66
4	r50-PEN-4	400 × 400		50	0.25	PEN	4	5.088	4.88
5	r50-PET-6	400 × 400		50	0.25	PET	6	5.046	4.84
6	r80	400 × 400	2	80	0.4	Control specimen	—	—	0
7	r80-PEN-2	400 × 400		80	0.4	PEN	2	2.544	2.41
8	r80-PEN-3	400 × 400		80	0.4	PEN	3	3.816	3.61
9	r80-PEN-4	400 × 400		80	0.4	PEN	4	5.088	4.82
10	r80-PET-6	400 × 400		80	0.4	PET	6	5.046	4.78

Resin-impregnated PEN FRP or PET FRP sheets were wrapped on the surface of the column through the wet-layup process, during which the fibers were oriented in the hoop direction and the overlapping zone was almost half the perimeter of the specimens. An additional three-layer CFRP strip with a width of 190 mm (0.165-mm nominal thickness per ply) was wrapped at the two ends of each specimen to avert undesired failure at these regions.

Material Properties

The ingredients of the concrete mix are detailed in Table 2. Three standard concrete cylinders with a diameter of 150 mm and a height of 300 mm were tested at the time of the column test to measure the properties of unconfined concrete per AS1012.9 (Standards Australia 2014). The peak axial stress (f'_c) and corresponding axial strain (ε'_c) are listed in Table 2.

The material properties of the reinforcements were obtained through tensile tests, and three steel bars were tested for each diameter of reinforcements according to BS 18 (BSI 1987). The stress–strain behavior and failure mode of the reinforcements are shown in Fig. 4. The mechanical properties of the steel bars are provided in Table 3.

Five PEN FRP and five PET FRP flat coupons were manufactured and tested per ASTM D3039/D3039M-17 (ASTM 2017) to measure the tensile properties, and the epoxy resin properties were provided by the manufacturer, as shown in Table 4. All coupons had a length of 250 mm and a width of 25 mm. The nominal thicknesses of PEN FRP and PET FRP fibers were 1.272 and 0.841 mm, respectively. The coupons were tested using the MTS universal testing machine [Fig. 5(a)] with a loading rate of 1.5 mm/min. A 20-mm strain gauge was mounted on the front and back of each coupon to monitor the tensile strain, and the load was determined by the test machine. Tensile stress was calculated using the nominal area of the LRS FRP fibers. Fig. 5(b) illustrates that the LRS FRP had a bilinear tensile stress–strain curve, which differs from the linear curves typically observed in conventional FRPs. The elastic modulus of the first linear segment is E_{frp1}, while the second linear segment's elastic modulus is E_{frp2}. ε_{frp0} is the strain where the elastic modulus changes. ε_{frp} and f_{frp} are the average tensile rupture strain and tensile stress from the flat coupon tests, respectively.

Test Setup and Instrumentation

As shown in Fig. 6(a), a total of six linear variable displacement transducers (LVDTs) were utilized to determine the axial strain of the column, with two LVDTs (LVDT-A and -B) measuring the overall axial shortening and four LVDTs measuring the axial deformation in the 500-mm mid-height portion. The layout of the strain gauges is depicted in Fig. 6(b). A 5-mm gauge length SG was mounted on each longitudinal reinforcement in the middle of the column. The hoop strains in the FRP jacket were measured using nine 20-mm gauge-length SGs on the jacket surface at the middle section of the column. These nine SGs were installed at three different locations outside the overlapping zone: (1) the middle width point of the three sides (2) the rounded corner's center; and (3) the transition point between the corner center and the adjacent sides (i.e., the location where the curvature changes).

Axial compression tests on all specimens were conducted using 72,000-kN capacity equipment at the Key Laboratory of Urban Security and Disaster Engineering of the Ministry of Education, Beijing University of Technology (Fig. 7). The test column was preloaded to about 20% of the anticipated ultimate load (i.e., the peak load) of the corresponding unconfined control specimen to check the alignment of the instrumentation and then was unloaded to zero force. Afterward, the axial load was exerted to the specimens with a displacement control rate of 0.6 mm/min. In the tests, strain gauge readings, loads from the test machine, and displacements from the LVDTs were simultaneously recorded by the digital logger.

Results and Discussions

Overall Behavior

The failure of the two control specimens, r50 and r80 [Figs. 8(a and f)], started with vertical cracks near the end region after reaching initial peak load, and then the cover concrete spalling and longitudinal reinforcement buckling occurred. It should be noted that the buckling of the longitudinal reinforcements in r50 occurred at the column's lower region [Fig. 8(a)]. Therefore, the same-end CFRP wrapping measures as given to those of the LRS FRP–confined specimens were taken for Specimen r80, and the near-end failure was successfully avoided [Fig. 8(f)]. Among the other eight axial-loaded LRS FRP–confined square RC columns, only one specimen, r50-PEN-2, failed by abrupt FRP rupture at the corner area near the column's midheight section [Fig. 8(b)]. This failure mode is similar to that commonly observed for small-scale square RC columns confined by the LRS FRP (Saleem et al. 2021), which indicates that the failure pattern is independent of the column size effect. When Specimen r50-PEN-2 failed, a very loud explosion occurred along with an observable shaking of the tester. Such failure for the remaining specimens with a thicker FRP jacket or larger corner radius might release more huge energy and, therefore, be risky for the testing machine and surroundings. Therefore, the compression tests of the remaining seven specimens

(a)

(b)

Fig. 3. Formwork fabrication: (a) steel cages; and (b) wooden molds.

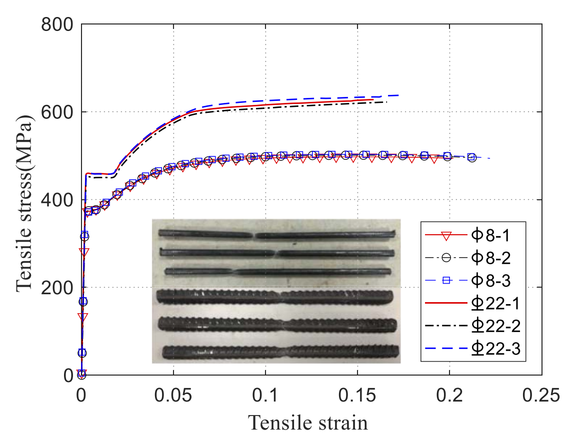

Fig. 4. Tensile stress–strain curves of reinforcements.

Table 2. Concrete mix proportions and properties

Concrete batch	Mix ratio (kg/m^3): Water	Cement	Sand	Aggregate	Fly ash	Ground granulated blast furnace slag	Water-reducing agent	Testing date compressive strength, f'_c (MPa): Average	SD	Testing date unconfined strain, ε'_c (%): Average	SD
C1	173	202	846	993	76	83	7.6	40.3	2.02	0.242	0.014

Table 3. Material properties of steel bars

Steel bar type	Diameter, d_s (mm)	Yield strength, f_y (MPa)	Ultimate strength, f_u (MPa)	Elastic modulus, E_s (GPa)	Yield strain, ε_y (%)	Ultimate strain, ε_u (%)
Longitudinal reinforcement (deformed steel bar)	22	454	646	197	0.23	16.59
SD	—	4.11	5.94	8.95	0.06	0.73
Transverse reinforcement (round steel bar)	8	372	500	177	0.21	21.17
SD	—	0.36	3.47	4.01	0.04	0.95

Table 4. Material properties of LRS FRP and epoxy resin

		Elastic modulus (GPa)								
		E_{frp1}		E_{frp2}			Ultimate strain, $\varepsilon_{\mathrm{frp}}$ (%)		Tensile strength, f_{frp} (MPa)	
Material	Thickness (mm)	Average	SD	Average	SD	$\varepsilon_{\mathrm{frp0}}$ (%)	Average	SD	Average	SD
PEN FRP	1.272	27.0	0.74	12.0	0.36	0.83	5.6	0.0131	714	84.7
PET FRP	0.841	17.9	0.42	8.3	0.34	0.68	8.2	0.0072	742	48.1
Epoxy resin (manufacturer)	—	2.6	—	—	—	—	1.9	—	40–50	—

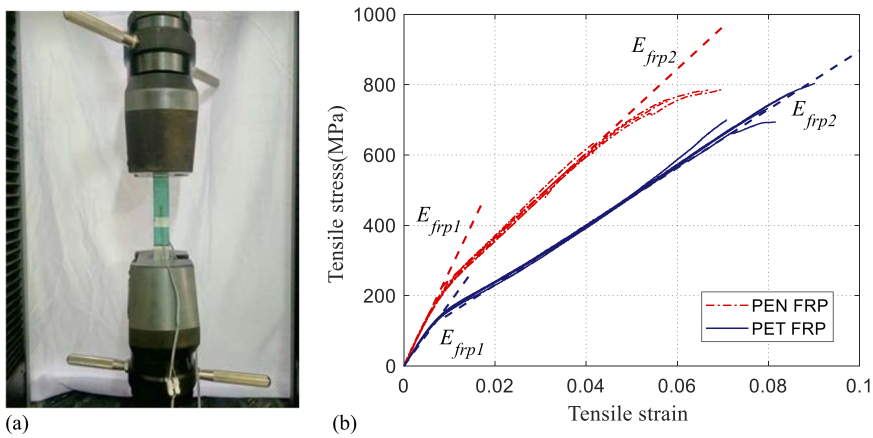

Fig. 5. Tensile test of LRS FRP flat coupons: (a) test setup; and (b) tensile stress–strain curves.

(r50-PEN-3, r50-PEN-4, r50-PET-6, r80-PEN-2, r80-PEN-3, r80-PEN-4, and r80-PET-6) were deliberately terminated before FRP rupture for safety reasons. The same actions were taken in previous large-scale tests in the authors' lab by Chan et al. (2021) and Bai et al. (2021a). This measure was achieved by monitoring the maximum hoop strain of the external FRP jacket. Once the monitored strain value reached the target values of 2.4% for PEN FRP and 3.2% for PET FRP, the test was stopped by hand. These target strain values were determined on the basis of the ultimate condition of Specimen r50-PEN-2 and a previous large-scale test in this lab (Bai et al. 2021a). It should be noted that the compressive test of r50-PEN-3 was terminated at a maximum FRP hoop strain of 1.9% due to an accident involving the test machine. This treatment was conservative, but it can still guarantee the main features of the compressive behavior (e.g., the trend of the last segment). The states at the termination point for all specimens were referred to as final conditions in this paper, and the photos of these conditions are shown in Fig. 8.

For all FRP-wrapped columns, local bulging and wrinkles of the FRP jacket occurred owing to the combined effect of axial compression and hoop tension [Figs. 8(c and d)]. To investigate the buckling conditions of the longitudinal steel bars, all FRP jackets were removed for the strengthened specimens after loading. It was found from Specimen r50-PEN-2 [Fig. 9(a)] that one longitudinal steel bar on the flat sides buckled more obviously than those on the rounded corners, which can be attributed to the fact that the confining pressure offered by the external FRP jacket is less on the middle flat side. This phenomenon is similar to the observations of conventional FRP-wrapped noncircular specimens (Wang and Wu 2011; Wang et al. 2016; Zeng et al. 2018). For the other specimens with a higher jacket stiffness, the longitudinal steel bars experienced only a very slight buckling as shown in Specimen R50-PEN-4 in Fig. 9(b). This indicates that buckling of longitudinal reinforcements in noncircular columns can be reasonably restrained by increasing FRP thickness.

Axial Stress–Strain Behavior of Concrete

The axial stress of concrete in this paper was defined as the average axial stress, determined by dividing the load acting on the concrete by its area. The ability of concrete to withstand the axial load was calculated by subtracting the axial load sustained by the longitudinal reinforcements from the overall axial load applied to the

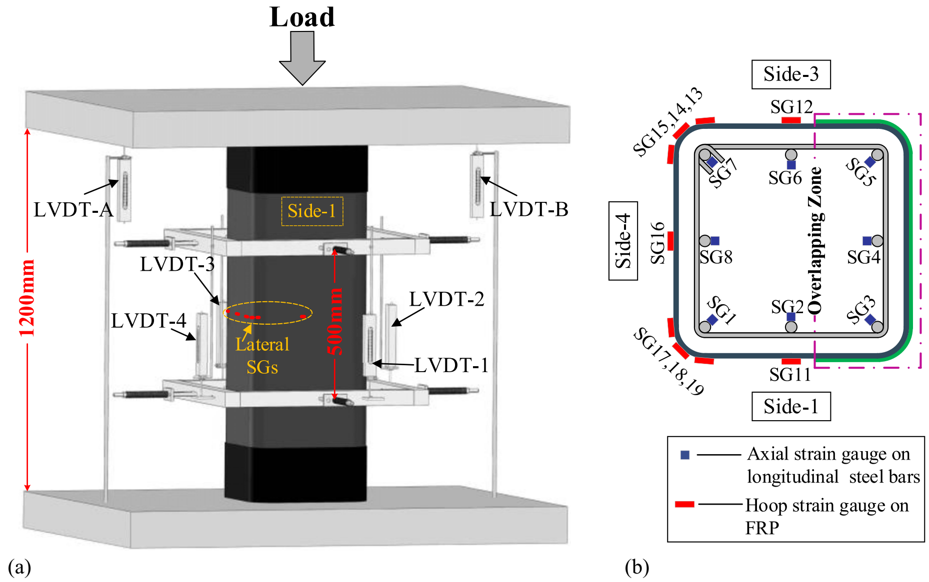

Fig. 6. Test setup: (a) layout of LVDTs; and (b) layout of strain gauges.

Fig. 7. Specimen during the test.

specimen. The former was obtained from the hypothetical perfect elastic–plastic stress–strain curve for longitudinal reinforcements. Similar methods have been used in previous research (Zeng et al. 2018, 2021). The axial strains of the specimens were determined by using the average values of four LVDT readings in the 500- mm portion of its middle height. The peak axial stresses of unconfined concrete, based on measurements of the control specimens, were 38.3 and 37.1 MPa for r50 and r80, respectively. The compressive stresses of concrete in the two unconfined large-scale control specimens were lower than the average compressive strength of standard concrete cylinders ($f'_c = 40.3$ MPa). This phenomenon has also been extensively reported and was mainly attributed to the possible size effect (De Luca et al. 2011; Zeng et al. 2018, 2021). In addition, different corner radii have almost no effect on the axial compressive strength of control specimens, which is similar to the observation on small-scale square columns with different corner radii (Han et al. 2020a). The average value of the two control specimens, 37.7 MPa, was adopted as the unconfined compressive strength (f'_{co}) for the large-scale specimens wrapped with FRP in this research unless otherwise specified, as shown in Table 5.

Fig. 10 depicts the different phases of a representative axial stress–strain scheme of concrete observed from the test curves, as shown in Figs. 11–13. The test curve can be divided into three branches in general: (1) the first ascending branch; (2) the initial strength–softening second branch; and (3) the final third branch. Notably, (f'_{c1}, ε_{c1}) is the initial peak point; (f'_{c2}, ε_{c2}) is the transition point; f'_{c2} is defined as the minimum stress for the initial strength–softening second branch; ($f'_{cu,f}$, $\varepsilon_{cu,f}$) is the final point corresponding to the final condition in this study; (f'_{cu}, ε_{cu}) is the ultimate point at FRP rupture. For ease of discussion, three basic ratios proposed by Lam and Teng (2003b) are introduced here: (1) the effective confinement ratio $k_s f_l / f'_{co}$; (2) the effective confinement stiffness ratio $\rho_{k,eff}$; and (3) the strain ratio ρ_ε. The first component, k_s, is the shape factor defined as the ratio of the effective confinement area to the total area of concrete. Because it is the second elastic modulus of the LRS FRP that acts during the later loading stage of the specimen, E_{frp2} is used to calculate these ratios for the purposes of comparison. The mathematical expressions of these ratios are

$$k_s \frac{f_l}{f'_{co}} = k_s \frac{2E_{frp2} t_{frp} \varepsilon_h}{f'_{co} d_e} = \rho_{K,eff} \rho_\varepsilon \tag{1}$$

$$\rho_{K,eff} = k_s \frac{2E_{frp2} t_{frp}}{(f'_{co}/\varepsilon_{co}) d_e} \tag{2}$$

$$\rho_\varepsilon = \frac{\varepsilon_h}{\varepsilon_{co}} \tag{3}$$

$$k_s = \frac{1 - ((b/h)(h-2r)^2 + (b/h)(b-2r)^2/(3A_g)) - \rho_{sc}}{1 - \rho_{sc}} \tag{4}$$

where ε_h = the hoop strain of the FRP jacket; f'_{co} = the compressive strength of the control RC specimen and ε_{co} = its corresponding

J. Compos. Constr., 2022, 26(4): 04022034

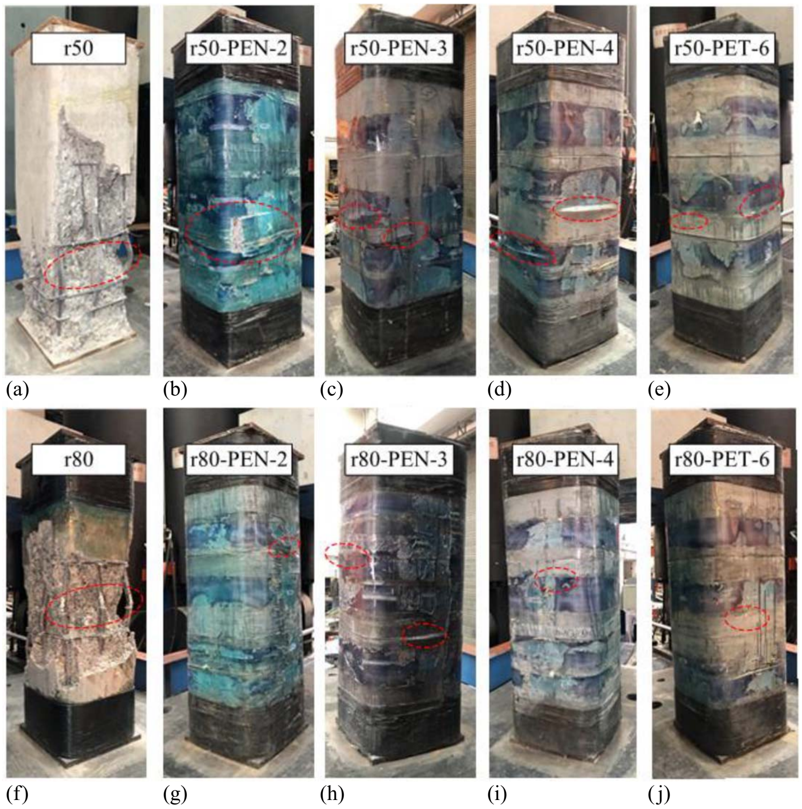

Fig. 8. Final conditions of test columns: (a) r50; (b) r50-PEN-2; (c) r50-PEN-3; (d) r50-PEN-4; (e) r50-PET-6; (f) r80; (g) r80-PEN-2; (h) r80-PEN-3; (i) r80-PEN-4; and (j) r80-PET-6.

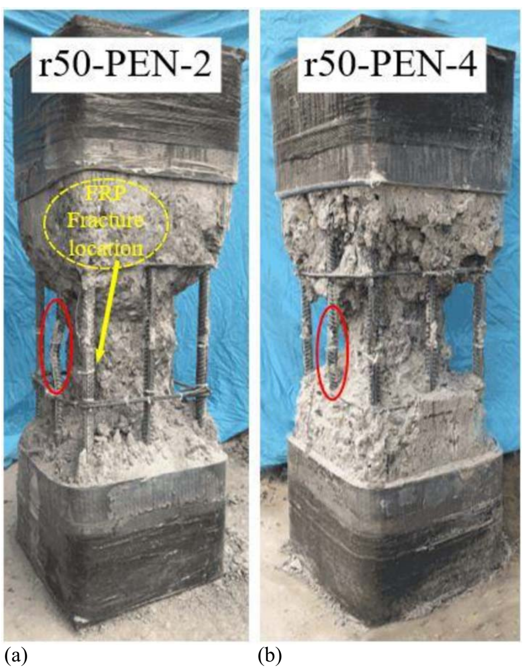

Fig. 9. Typical buckling mode: (a) r50-PEN-2; and (b) r50-PEN-4.

axial strain; ρ_{sc} = the longitudinal steel reinforcement ratio; d_e = the equivalent diameter of the cross section, which is defined by $d_e = \sqrt{h^2 + b^2}$; and A_g = the gross area of the column section with rounded corners, which is defined by $A_g = bh-(4-s\pi)r^2$. These symbols and terminology will be used throughout the subsequent discussion unless otherwise specified.

In Figs. 11–13, the stress values corresponding to different average hoop strains at the corner center for the external FRP jacket are presented by various scatter points to facilitate the comparison. As expected, the test curve's first parabolic rising branch is almost identical with that of an unconfined control specimen. Because there was no damage or expansion in the concrete during the initial loading stage, the FRP jacket was not activated. However, after reaching the initial peak point for the specimen, the last two segments of the test curves are substantially affected by the number of FRP layers and corner radius. It is seen that the second branch for most of the specimens exhibited a stress reduction (referred to as the initial strength–softening behavior), which is due to the low effective confinement stiffness ratio. As damage to the concrete saw a progressive increase, the descending trend of the curves slowed down and stopped at one point when the effective confinement ratio reached a level that could sufficiently confine the concrete in the large-scale columns. This point is equal to the transition point (f'_{c2}, ε_{c2}) on the representative curve illustrated in Fig. 10. Beyond this point, increasing the axial strains resulted in either a nearly flat or slightly rising final branch in the test columns' stress–strain curves. However, when the effective confinement stiffness ratio exceeded a certain threshold, the first ascending portion was followed by an ascending segment without initial strength loss (referred to as the hardening behavior, which occurred in Specimen r80-PEN-4). It should be stated that the stress at the end of the first ascending segment of Specimen r80-PEN-4 was smaller than the initial peak stress of other specimens where initial strength loss occurred (e.g., r50-PEN-4). This might be attributed to the local concrete damage observed in the specimen near the peak load.

Table 5 summarizes the key test findings in detail. For Specimen r50-PEN-2, which experienced FRP rupture failure, the final point

Table 5. Key test results of specimens

No.	Specimen	f'_c (MPa)	f'_{co} (MPa)	f'_{c1} (MPa)	f'_{c2} (MPa)	$f'_{cu,f}$ (MPa)	f'_{cc} (MPa)	$f'_{c1}-f'_{c2}$ (MPa)	ε_{co} (%)	$\varepsilon_{cu,f}$ (%)	E'_2 (MPa)	k_s	$\rho_{K,\mathrm{eff}}$
1	r50	40.3	38.3	—	—	—	38.3	—	0.25	—	—	0.6124	—
2	r50-PEN-2	40.3	37.7	44.8	28.1	28.6	44.8	16.7	0.25	1.94	90	0.6124	0.0062
3	r50-PEN-3	40.3	37.7	45.9	33.1	37.6	45.9	12.8	0.25	2.65	220	0.6124	0.0093
4	r50-PEN-4	40.3	37.7	46.9	38.1	42.1	46.9	8.8	0.25	2.85	190	0.6124	0.0124
5	r50-PET-6	40.3	37.7	48.5	33.9	35.3	48.5	14.6	0.25	2.31	92	0.6124	0.0085
6	r80	40.3	37.1	—	—	—	37.1	—	0.25	—	—	0.7465	—
7	r80-PEN-2	40.3	37.7	44.2	36.6	38.2	44.2	7.6	0.25	1.53	213	0.7465	0.0076
8	r80-PEN-3	40.3	37.7	44.8	38.6	42.4	44.8	6.2	0.25	2.73	230	0.7465	0.0113
9	r80-PEN-4	40.3	37.7	—	—	47.9	47.9	—	0.25	2.34	274	0.7465	0.0151
10	r80-PET-6	40.3	37.7	47.6	38.1	39.9	47.6	9.5	0.25	1.97	190	0.7465	0.0104

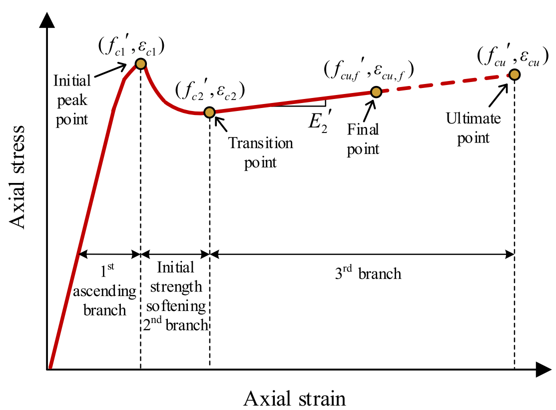

Fig. 10. Illustration of a typical axial stress–strain curve.

was equal to the ultimate point illustrated in Fig. 10. For Specimen r80-PEN-4 with hardening behavior, the transition point did not appear and, therefore, could not be presented. f'_{cc} was the maximum axial stress for each test column, and $f'_{c1}-f'_{c2}$ was defined as the initial strength loss. In addition, the final segment slope (E'_2), calculated as $E'_2 = (f_{cu,f} - f'_{c2})/(\varepsilon_{cu,f} - \varepsilon_{c2})$, together with the shape factor and effective confinement stiffness ratio of all specimens, is given in Table 5. The aforementioned figures and the findings provided in Table 5 show that the amount of FRP and corner radius play a vital role in the compressive performance of LRS FRP–jacketed large-scale specimens. In the next sections, the effects of the major test parameters of this paper will be carefully investigated.

Effect of Corner Radius

The effect of the corner radius on the axial stress–strain responses of concrete is shown in Fig. 11. Clearly, the specimen with the small corner radius usually has a larger axial strain at a given hoop strain. This is because the smaller the corner radius of the noncircular specimen is, the more obvious the stress concentration at the corner will be. Besides, the specimens with a corner radius of 80 mm have less strength loss along the second branch than that of the specimens with a 50-mm corner radius. This implies that increasing the corner radius can reduce the specimens' initial strength loss. The magnitude of the initial strength loss is more pronounced for the columns wrapped with two layers of PEN FRP. However, as shown in Fig. 11(c), it is found that the initial strength loss can be avoided when the number of PEN FRP layers is increased to four layers for Specimen r80-PEN-4. Fig. 11 also shows that increasing the corner radius generally leads to a slight rise of the slope for the last branch of the curve. Table 5 shows that Specimens r50-PEN-3 and r80-PEN-2 have similar effective confinement stiffness ratios, so that the slopes of the last branch of their curves are close to each other (i.e., 220 and 213 MPa, respectively). This indicates that the final portion's slope is highly correlated with the effective confinement stiffness ratio, which is affected by the corner radius and the number of FRP layers. The aforementioned findings illustrate the interaction between the impacts of the corner radius and FRP thickness on the column behavior.

Effect of FRP Thickness

Fig. 12 depicts the impact of FRP jacket thickness on the axial stress–strain curves of the specimens. For a given hoop strain, the axial strain of the test column is substantially impacted by FRP thicknesses from two to three and four layers. This significant comparison could be attributed to the lower effective confinement stiffness ratio of the two layers of PEN FRP for the large-scale specimen, which leads to the rapid expansion of concrete. On the other hand, Fig. 12 and the findings presented in Table 5 illustrate that the FRP amount has negligible effect on the initial peak stress of the specimen. However, Table 5 reveals that the initial stress loss is closely related to the stiffness of the external FRP jacket; the magnitude of stress reduction decreases with the rise of the FRP layers. Furthermore, Table 5 shows that for Specimens r50-PEN-2 and r50-PEN-3, the slope change of the final portion obviously increases with the FRP layers. When the confinement stiffness ratio is greater than a certain value, the slope change is not obvious. This view is confirmed by the comparison of Specimens r50-PEN-3 and r50-PEN-4 and also the comparison of Specimens r80-PEN-2 and r80-PEN-3.

Effect of FRP Types

Fig. 13 compares the axial stress–strain behavior of test columns confined by PEN FRP and PET FRP. The columns displayed in Figs. 13(a and b) have the same corner radius and nearly similar effective confinement stiffness ratios (0.0093 for r50-PEN-3 and 0.0085 for r50-PET-6, as well as 0.0113 for r80-PEN-3 and 0.0104 for r80-PET-6) as reported in Table 5. As previously discussed, the compressive response of concrete is highly related to the effective confinement stiffness ratio. Both Fig. 13 and Table 5 confirm that the magnitude of stress reduction along the second branch of the specimens is similar for two different kinds of FRP. The final branches of Specimens r50-PEN-3 and r50-PET-6 are very close, while those of Specimens r80-PEN-3 and r80-PET-6 are almost identical with each other. It should be noted that the final axial strain of the column confined with PET FRP is smaller than that confined with PEN FRP. The reason for this is that the experiment was intentionally stopped early without the ultimate condition of FRP rupture. Just like the observation for small-scale specimens with different LRS FRPs made by Han et al. (2020a, b), it can be expected that the ultimate axial strain of the large-scale specimen confined with PET FRP should be greater

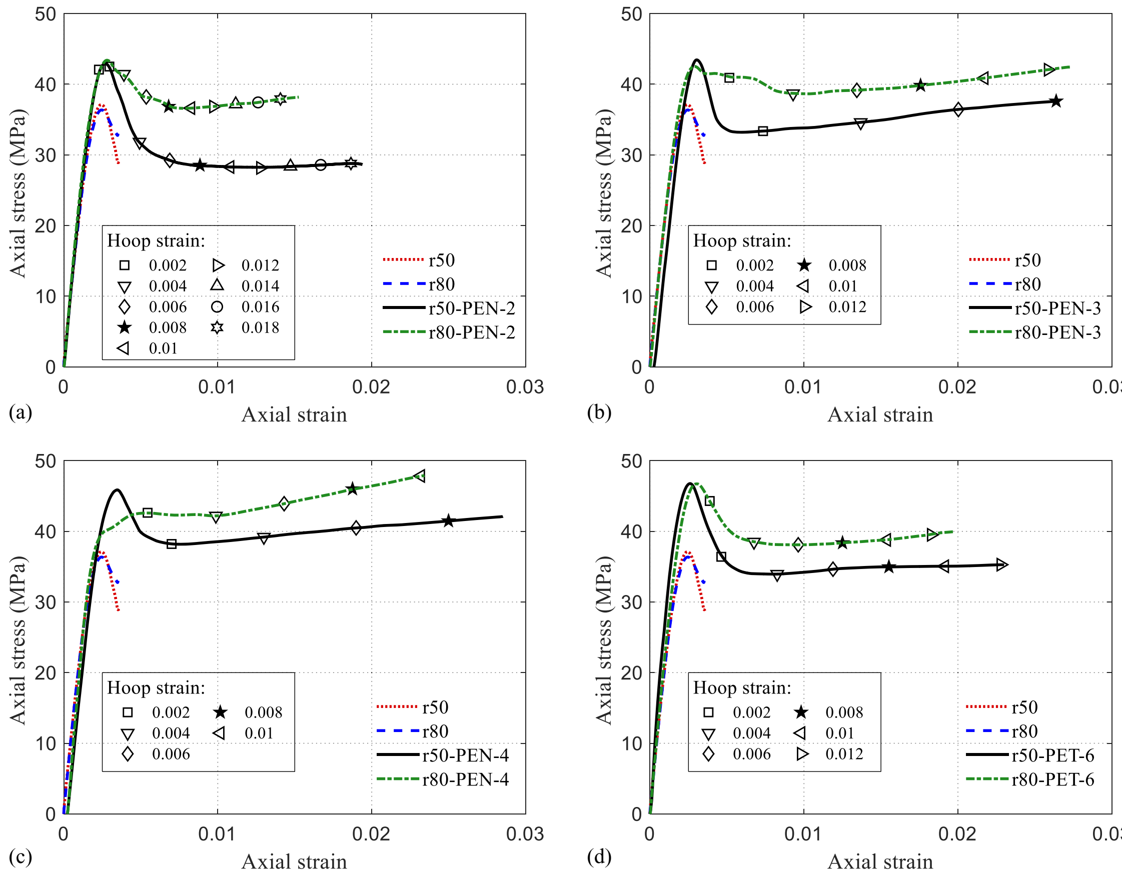

Fig. 11. Effect of the corner radius on axial stress–strain curves: (a) $N_{\mathrm{frp}} = 2$, PEN FRP; (b) $N_{\mathrm{frp}} = 3$, PEN FRP; (c) $N_{\mathrm{frp}} = 4$, PEN FRP; and (d) $N_{\mathrm{frp}} = 6$, PET FRP.

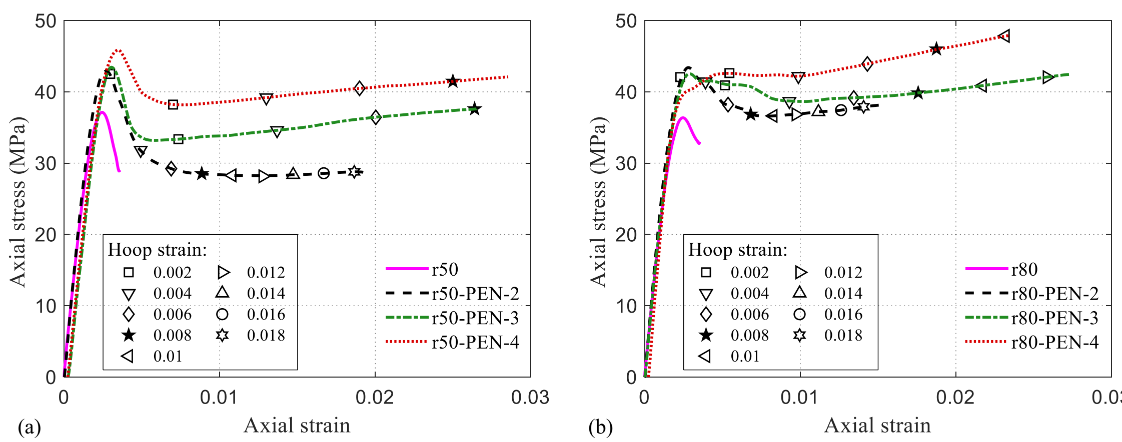

Fig. 12. Effect of FRP thickness on axial stress–strain curves: (a) $r = 50$, PEN FRP; and (b) $r = 80$, PEN FRP.

than that of the column confined with PEN FRP at FRP rupture when the jacket stiffness is close to each other. Because the tensile rupture strain of PET FRP is greater than that of PEN FRP, it is reasonable to expect that PET FRP–reinforced structures will have better ductility performance in practical applications.

Hoop Strains at Final Condition

Fig. 14 depicts the hoop strain variations around the cross section for the tested specimens (outside the overlap region) in their final condition. All these hoop strains were determined using SGs mounted on the external FRP jacket at the midsection of the specimens. The value with a box mark stands for the largest FRP hoop strain. Notably, the peak value of the hoop strain for FRP mostly appears on the middle part of the flat side. However, FRP fracture usually happened at or close to one of the transition points, rather than in the region of the largest FRP hoop strain as is the case with r50-PEN-2 in Fig. 14(a). Other scholars have presented the same findings (Zeng et al. 2018; Han et al. 2020a; Saleem et al. 2017, 2021; Chan et al. 2021). The expansion of concrete on the column's flat sides is more obvious than that at the rounded corners

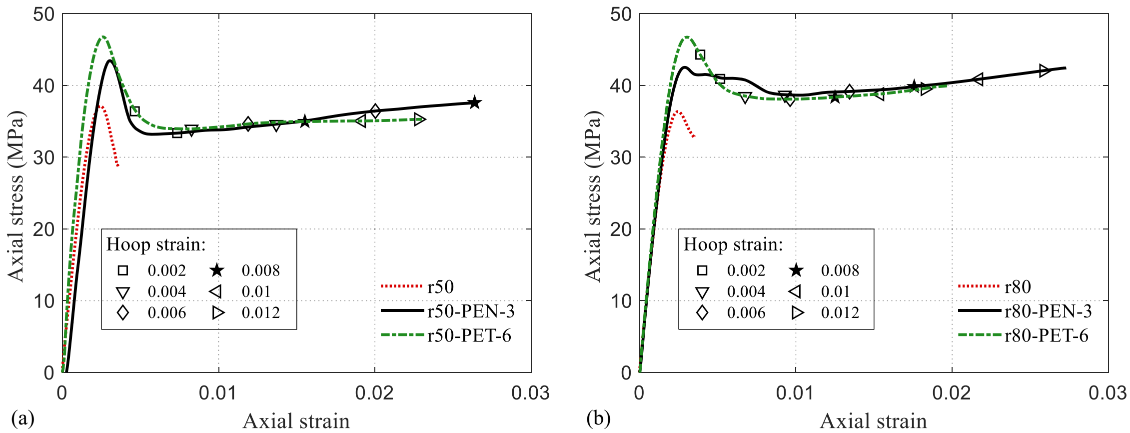

Fig. 13. Effect of FRP type on axial stress–strain curves: (a) $r = 50$; and (b) $r = 80$.

because the flexural stiffness of the flat sides is much smaller (Zeng et al. 2018). The nonuniform expansion of the confined concrete resulted in a significant flexural strain in the outer FRP, with the maximum flexural strain occurring at the transition points of the curvature change, which interprets the position of the FRP fracture. It can also be observed from Fig. 14 that, compared with the other preterminated specimens without FRP rupture, the difference in the circumferential strain of Specimen r50-PEN-2 at FRP rupture is much less apparent. The reason may be that the specimen confined by the LRS FRP must undergo a large deformation prior to FRP fracture, so its square cross section tends to progressively approach a circle as the axial load increases, making the stress distribution more uniform with the development of the axial deformation. Moreover, a careful inspection of the two counterpart specimens with different corner radii (e.g., r50-PEN-2 and r80-PEN-2; r50-PEN-4 and r80-PEN-4; and r50-PET-6 and r80-PET-6) reveals that the maximum hoop strain at the final point increases with the growth of the corner radius, which reduces the stress concentration and, therefore, leads to a more uniform circumferential strain distribution.

LRS FRP–Confined Concrete Models with Square Cross Sections

General

Today, two monotonic stress–strain models are available for LRS FRP–confined concrete in noncircular columns (Pimanmas and Saleem 2019; Zhang 2021). Both of them are design-oriented models and were established on the basis of the experimental results of small-scale LRS FRP–confined noncircular columns. Pimanmas and Saleem (2019) presented the first LRS FRP–confined concrete model for noncircular columns. As previously illustrated in Fig. 10, the experimental axial stress–strain curve is divided into three branches. Pimanmas and Saleem (2019) adopted two transition segments for their model, which depict the initial strength–softening branch of the test curve and intersect at the transition point (f'_{cs}, ε_{cs}). Therefore, this model consists of four segments and four control points. A definition of the control points is given in Table 6. The framework of the stress–strain curve is as follows:

1. The first ascending branch ($0 < \varepsilon_c < \varepsilon_{c1}$) is expressed as follows:

$$f_c = E_c\varepsilon_c\left[1 - \frac{1}{n}\left(\frac{\varepsilon_c}{\varepsilon_{c1}}\right)^{n-1}\right] \tag{5}$$

where f_c and ε_c = axial stress and strain of concrete in the LRS FRP–confined specimen; and n = coefficient and is given by

$$n = \frac{E_c\varepsilon_{c1}}{E_c\varepsilon_{c1} - f'_{c1}} \tag{6}$$

where E_c = initial tangent modulus of unconfined concrete and is calculated from an ACI 318-19 (ACI 2019) equation ($E_c = 4{,}700\sqrt{f'_{co}}$).

2. The second transition segment ($\varepsilon_{c1} < \varepsilon_c < \varepsilon_{cs}$) is written

$$f_c = \frac{Kf'_{c1}(\varepsilon_c/\varepsilon_{c1})}{1 + A(\varepsilon_c/\varepsilon_{c1}) + B(\varepsilon_c/\varepsilon_{c1})^2 + C(\varepsilon_c/\varepsilon_{c1})^3} \tag{7}$$

where A, B, C, and K = coefficients and are defined by

$$A = C + K - 2 \tag{8}$$

$$B = 1 - 2C \tag{9}$$

$$C = K\frac{((f'_{c1}/f'_{cs}) - 1)}{((\varepsilon_{cs}/\varepsilon_{c1}) - 1)^2} - \frac{\varepsilon_{c1}}{\varepsilon_{cs}} \tag{10}$$

$$K = \frac{E_c}{E_{\text{sec}}} \tag{11}$$

where E_{sec} = secant modulus and is calculated by

$$E_{\text{sec}} = \frac{f'_{c1}}{\varepsilon_{c1}} \tag{12}$$

3. The third transition segment ($\varepsilon_{cs} < \varepsilon_c < \varepsilon_{c2}$) is given as follows:

$$f_c = f'_{cs} - E_2(\varepsilon_{c2} - \varepsilon_{cs}) \tag{13}$$

where E_2 = slope of the third transition part and is given by

$$E_2 = \frac{f_{cs} - f'_{c2}}{\varepsilon_{c2} - \varepsilon_{cs}} \tag{14}$$

4. The final branch ($\varepsilon_{c2} < \varepsilon_c < \varepsilon_{cu}$) is expressed as follows:

$$f_c = f'_{c2} + E_3(\varepsilon_{cu} - \varepsilon_{c2}) \tag{15}$$

where E_3 = slope of the last part and is calculated as follows:

$$E_3 = \frac{f'_{cu} - f'_{c2}}{\varepsilon_{cu} - \varepsilon_{c2}} \tag{16}$$

Based on the framework by Pimanmas and Saleem (2019) and a database of LRS FRP–wrapped circular and noncircular specimens,

J. Compos. Constr., 2022, 26(4): 04022034

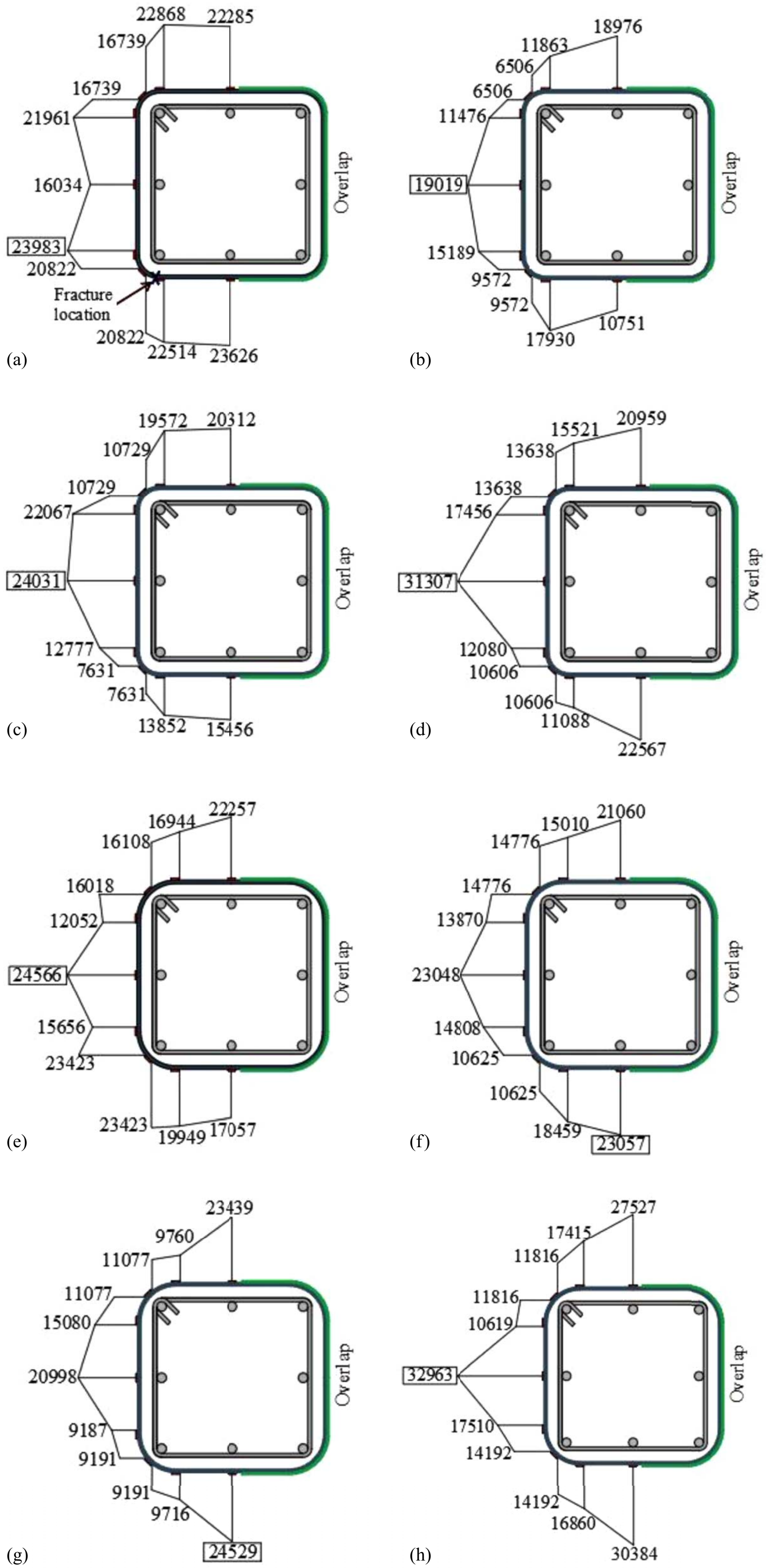

Fig. 14. FRP hoop strain distributions at the final condition (unit: με): (a) r50-PEN-2; (b) r50-PEN-3; (c) r50-PEN-4; (d) r50-PET-6; (e) r80-PEN-2; (f) r80-PEN-3; (g) r80-PEN-4; and (h) r80-PET-6.